nature nanotechnology

LETTERS

PUBLISHED ONLINE: 4 JULY 2016 | DOI: 10.1038/NNANO.2016.108

# A charge-density-wave oscillator based on an integrated tantalum disulfide–boron nitride–graphene device operating at room temperature

Guanxiong Liu[1], Bishwajit Debnath[2], Timothy R. Pope[3], Tina T. Salguero[3], Roger K. Lake[2] and Alexander A. Balandin[1]*

**The charge-density-wave (CDW) phase is a macroscopic quantum state consisting of a periodic modulation of the electronic charge density accompanied by a periodic distortion of the atomic lattice in quasi-1D or layered 2D metallic crystals[1–4]. Several layered transition metal dichalcogenides, including 1T-$TaSe_2$, 1T-$TaS_2$ and 1T-$TiSe_2$ exhibit unusually high transition temperatures to different CDW symmetry-reducing phases[1,5,6]. These transitions can be affected by the environmental conditions, film thickness and applied electric bias[1]. However, device applications of these intriguing systems at room temperature or their integration with other 2D materials have not been explored. Here, we demonstrate room-temperature current switching driven by a voltage-controlled phase transition between CDW states in films of 1T-$TaS_2$ less than 10 nm thick. We exploit the transition between the nearly commensurate and the incommensurate CDW phases, which has a transition temperature of 350 K and gives an abrupt change in current accompanied by hysteresis. An integrated graphene transistor provides a voltage-tunable, matched, low-resistance load enabling precise voltage control of the circuit. The 1T-$TaS_2$ film is capped with hexagonal boron nitride to provide protection from oxidation. The integration of these three disparate 2D materials in a way that exploits the unique properties of each yields a simple, miniaturized, voltage-controlled oscillator suitable for a variety of practical applications.**

The 1T polytype of $TaS_2$ undergoes the transition from a normal metallic phase to an incommensurate CDW (IC-CDW) phase at 545 K, to a nearly commensurate CDW (NC-CDW) phase at 350 K and, finally, to a commensurate CDW (C-CDW) phase at 180 K (refs 7–11). Each phase transition is accompanied by a lattice reconstruction, which results in strong modifications to the material's electrical properties. In 1T-$TaS_2$, the C-CDW phase drives a Mott–Hubbard metal-to-insulator transition (MIT) that results in a Mott insulating state. Intercalation and doping, the ambient pressure, the thickness of the quasi-2D films, optical excitation and the applied electric source–drain and gate bias can modify the transitions to different CDW phases[7–16]. For example, when the thickness of the 1T-$TaS_2$ film is <10 nm, the C-CDW–NC-CDW transition at 180 K disappears, whereas the NC-CDW–IC-CDW transition at 350 K persists[10]. A source–drain voltage can trigger the phase transition. In the case of 1T-$TaS_2$ the electrical conductivity abruptly increases when the applied electric field exceeds 20 kV $cm^{-1}$, which is attributed to the insulator-to-metal transition (IMT)[14]. A reverse MIT is revealed when the voltage is swept back[14]. Despite great recent interest in the CDW properties of quasi-2D transition metal dichalcogenides[10–12,14,17], neither the IMT nor the MIT induced by an electric field have been observed above room temperature. Correspondingly, no devices that use CDW transitions as the basis of their operation have been demonstrated at or near room temperature.

In this work, we show that an abrupt change in the electrical conductivity and hysteresis observed at the IMT and MIT transitions associated with the transition between the NC-CDW and IC-CDW phases in a quasi-2D 1T-$TaS_2$ channel can be used to construct an oscillator that operates at room temperature and up to 320 K. A second quasi-2D material, hexagonal boron nitride (h-BN), provides environmental protection against oxidation and preserves the CDW phase. A third integrated 2D material, graphene, provides a transistor with a current density and load resistance that closely match to $TaS_2$, allowing precise voltage control of the oscillator frequency. The voltage-controlled oscillator (VCO) demonstrated here does not require a complicated biasing circuit and could lead to inexpensive technologies for communication systems and other applications.

High-quality 1T-$TaS_2$ crystals were prepared by the chemical vapour transport method (see Methods). The prototype devices were fabricated with exfoliated thin films. To protect the exfoliated 1T-$TaS_2$ from oxidation we used an h-BN capping layer positioned on top of the CDW channel[18,19]. The fabricated devices consisted of 1T-$TaS_2$ channels with depth in the range of 6–9 nm and Pd/Au (15/60 nm) contacts. An optical image of a typical device is shown in an inset in Fig. 1b (see also Supplementary Figs 1–6). Figure 1a shows the current–voltage ($I$–$V$) characteristics of such $TaS_2$-BN devices in the temperature range from 78 to 395 K, which includes the 1T-$TaS_2$ phase transition from the NC-CDW to IC-CDW states. Below 320 K, we observe a prominent abrupt current jump as the voltage exceeds a certain value, denoted here as $V_H$. This behaviour is also referred to as threshold switching between the low and high conductivity states. When the voltage is swept back to zero, a reverse threshold switch occurs at a lower voltage $V_L$ that corresponds to a smaller critical electric field. The difference between these two voltages forms a hysteresis window. Details extracted from Fig. 1a are shown in Supplementary Fig. 4. It is important to note that the threshold switching effect in our device exists throughout the temperature range from 78 to 320 K. As the temperature is increased to 345 K, slightly below the transition from NC-CDW to IC-CDW at 350 K, threshold switching becomes weak (inset, Fig. 1a). Increasing the temperature above 350 K

[1]Department of Electrical and Computer Engineering, Nano-Device Laboratory (NDL) and Phonon Optimized Engineered Materials (POEM) Center, University of California – Riverside, Riverside, California 92521, USA. [2]Department of Electrical and Computer Engineering, Laboratory for Terascale and Terahertz Electronics (LATTE), University of California – Riverside, Riverside, California 92521, USA. [3]Department of Chemistry, University of Georgia, Athens, Georgia 30602, USA. *e-mail: balandin@ece.ucr.edu



© 2016 Macmillan Publishers Limited, part of Springer Nature. All rights reserved.

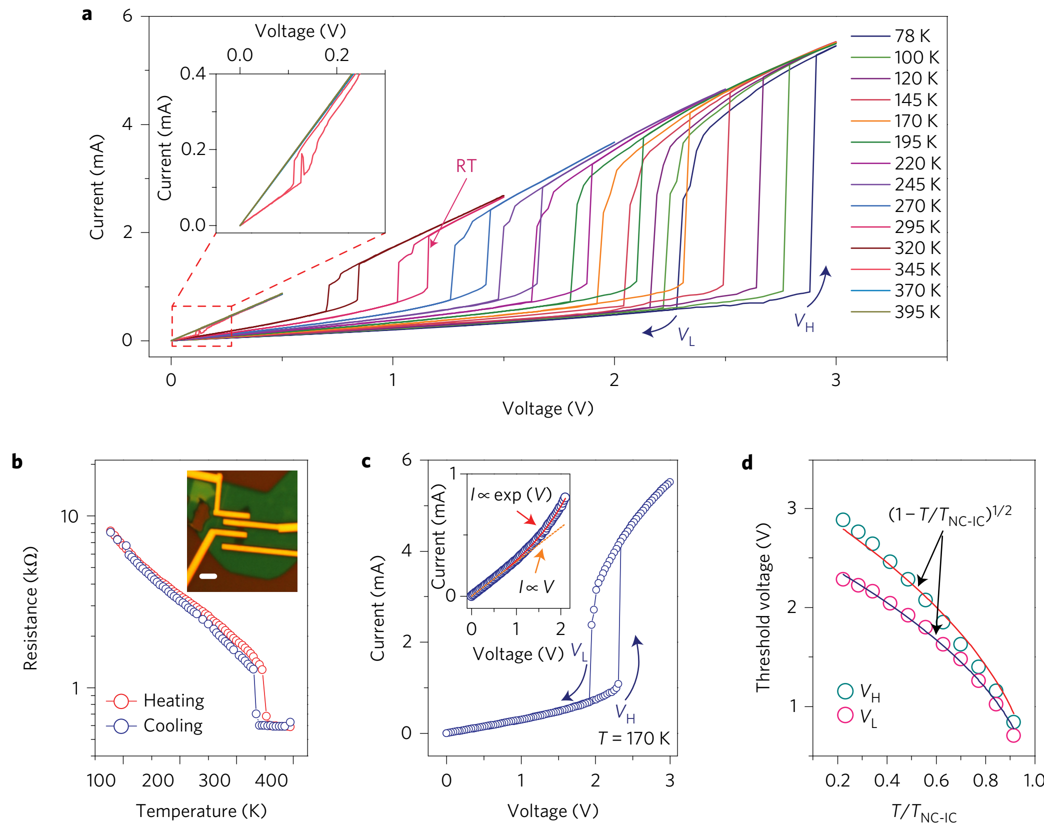


**Figure 1 | Electrical characteristics of thin-film 1T-$TaS_2$.** **a**, *I*–*V* characteristics of thin-film 1T-$TaS_2$ at different temperatures from 78 to 395 K. The threshold switching effect is prominent from 78 to 320 K. The blue arrows indicate the voltage sweep direction for the measurement at 78 K. For all other temperatures $V_H$ is always higher than $V_L$. The hysteresis window is defined as $V_H–V_L$. The threshold switching is prominent up to 320 K, and becomes less pronounced as the temperature approaches the NC-CDW–IC-CDW transition at 350 K. As shown in the inset, at 345 K the threshold switching is still measurable. As the temperature exceeds 350 K, the *I*–*V* slope becomes linear. **b**, Temperature-dependent resistance measurements for a 9-nm-thick 1T-$TaS_2$ film. The NC-CDW–IC-CDW and IC-CDW–NC-CDW transitions happen at 350 and 340 K during the heating and cooling processes, respectively. The resistance is measured at a low voltage ($V$ = 20 mV). Inset: An optical image of a typical h-BN-capped 1T-$TaS_2$ device. The dark purple strip is the 1T-$TaS_2$ thin film and the larger green region is the h-BN film. Scale bar, 5 μm. **c**, Superlinear *I*–*V* characteristics below $V_H$. The curve at $T$ = 170 K is shown here as an example. Arrows indicate the voltage sweeping directions. Inset: The current below $V_H$ can be fitted with an exponential component $I \propto \exp(V)$ superimposed on a linear curve $I \propto V$. **d**, Temperature-dependent threshold switching voltage. Both $V_H$ and $V_L$ are proportional to $(1–T/T_{NC\text{-}IC})^{1/2}$, a dependency that is identical to that described by analytical theories of the CDW order parameter[1].

results in the disappearance of threshold switching and the *I*–*V* characteristics become linear as the 2D 1T-$TaS_2$ channel enters the IC-CDW phase. Figure 1b presents the temperature-dependent resistance measured with a small voltage (20 mV). The resistance decreases as temperature increases until the NC-CDW–IC-CDW transition point near 350 K is reached, where the resistance drops abruptly. After the transition the resistance becomes almost constant with temperature. In the cooling cycle, the resistance jump occurs at 340 K, forming a temperature hysteresis. The absence of a C-CDW to NC-CDW phase transition at 180 K in very thin films (<9 nm) of 1T-$TaS_2$ is consistent with a recent report[10].

Another interesting observation is that the resistance value after electrically induced switching is the same for all temperatures, as seen from the similar slopes of the *I*–*V* curves at high field in Fig. 1a. The resistance extracted from the slope is 580 Ω, which matches the low-field temperature-dependent resistance of 590 Ω presented in Fig. 1b at $T > 350$ K. In addition, the low-field resistances extracted at lower temperatures from the *I*–*V* slopes in Fig. 1a are also in agreement with the measured resistance in Fig. 1b, shown in Supplementary Fig. 8. This equivalence in resistance values is consistent with the picture of voltage-controlled switching driving the 1T-$TaS_2$ between the NC-CDW and the IC-CDW phases. Another possibility is that the applied field and the resulting current destroy the Mott insulating state within the individual CDW domains while leaving the lattice in the NC-CDW phase. We also note that the threshold switching voltage scales linearly with the channel length (Supplementary Fig. 5). The critical fields $E_H$ and $E_L$ are 28.8 and 22.8 kV cm$^{-1}$ at 78 K and decrease to 11.2 and 10.2 kV cm$^{-1}$ at room temperature. The length scaling suggests a possibility of further reductions of the threshold voltage for devices with shorter channels.

We observe that the *I*–*V* characteristics below $V_H$ do not have a simple linear dependence. Instead there is an extra exponential component as shown in Fig. 1c. The temperature dependence of the threshold voltages $V_H$ ($V_L$) follows the relation $(1–T/T_{NC\text{-}IC})^{1/2}$ below the NC-CDW–IC-CDW transition temperature of 350 K (see Fig. 1d). This temperature dependence is the same as that described by analytical theories of the CDW order parameter[1] and has recently been observed in 2H-$TaS_2$ (ref. 20).

By connecting this 1T-$TaS_2$ device with an off-chip $R_L$ = 1 kΩ load resistor (see the schematic in Fig. 2a), we observe stable voltage oscillation at the node between these two components when applying a d.c. bias $V_{DC}$. These voltage oscillations, monitored by an oscilloscope, are shown in Fig. 2b. The initiation of oscillations requires $V_{DC}$ values within a certain range. When $V_{DC}$ is below 3.8 V no oscillations occur. As $V_{DC}$ increases, the oscillations



© 2016 Macmillan Publishers Limited, part of Springer Nature. All rights reserved.

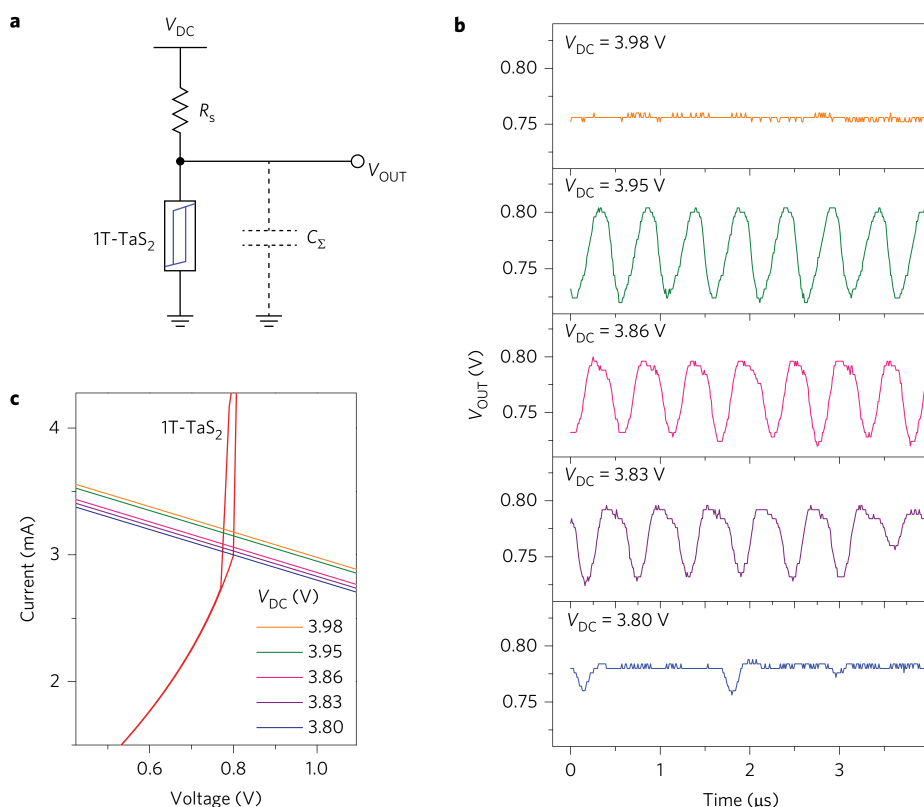


**Figure 2 | Oscillator circuit of a 1T-TaS$_2$ film with an off-chip load resistor. a**, The circuit diagram of the oscillator consists of the 1T-TaS$_2$ film, a series-connected load resistor and a lumped capacitance $C_\Sigma$ from the output node $V_{OUT}$ to ground. The load resistance is 1 kΩ. The output terminal is monitored by an oscilloscope. **b**, Voltage oscillations under different $V_{DC}$ values. The circuit oscillates when $V_{DC}$ is within the range of 3.83 V to 3.95 V. The oscillation frequencies are approximately 1.77, 1.85 and 2 MHz when $V_{DC}$ is 3.83, 3.86 and 3.95 V, respectively. **c**, Load lines of the resistor at different $V_{DC}$ values. The blue line, which represents $V_{DC}$ = 3.8 V, intersects with $V_H$ of 1T-TaS$_2$. This is the condition at which the circuit is about to oscillate.

become sinusoidal. The oscillation frequency, $f$, is dependent on $V_{DC}$. In this specific device $f$ was tuned from 1.77 to 2 MHz as $V_{DC}$ changed from 3.83 to 3.95 V. When $V_{DC}$ becomes greater than 3.98 V, the oscillation stops. The oscillation mechanism can be understood as the switching of the 1T-TaS$_2$ device between the IMT and MIT states with the negative feedback from the load resistor $R_L$. When $V_{DC}$ is large enough, the d.c. voltage across the 1T-TaS$_2$ channel reaches $V_H$ and triggers the IMT. The sudden increment in current results in a large voltage increase across the load resistor. As $V_{DC}$ is constant, the instantaneous voltage across the 1T-TaS$_2$ decreases, driving 1T-TaS$_2$ back into the insulating state. The current then decreases, reducing the voltage across the resistor and increasing the voltage across 1T-TaS$_2$, driving it back into its metallic state. As long as this voltage can increase to a level higher than $V_H$ the cycle keeps repeating. Figure 2c provides further explanation. The intersection of the 1T-TaS$_2$ curve with the load line is the operation d.c. voltage at the output. The line representing $V_{DC}$ = 3.8 V is on the edge of $V_H$, where the oscillations just start. As the oscillation is triggered by IMT–MIT processes, it also can be observed at lower temperature (Supplementary Fig. 6).

Voltage control of an oscillator frequency using simple circuitry is highly desirable for numerous miniaturized electronic systems. Conventional VCOs usually require multiple transistors and resistors for biasing[21,22]. By monolithically integrating a top-gate graphene field-effect transistor (G-FET) with an h-BN capped 1T-TaS$_2$ device, we demonstrate a VCO operating at room temperature. The gate and contact electrodes for this 2D integrated TaS$_2$–h-BN–graphene oscillator were fabricated with electron beam lithography, dry etching and metal evaporation (Supplementary Fig. 3). The device structure and SEM image are presented in Fig. 3a (bottom),b, respectively. The equivalent circuit and the biasing scheme are shown in Fig. 3a (top). The d.c. bias is applied across the integrated structure whereas the gate voltage of the G-FET is used to change $R_L$ and hence tune the oscillation frequency. Note that both the 1T-TaS$_2$ and graphene sides of the channel are contacted from the edge, forming quasi-1D contacts[18,23]. The h-BN entirely covers the 1T-TaS$_2$ and graphene sides of the channel to protect against environmental exposure.

The resulting device demonstrates excellent control of the oscillations using the gate voltage, $V_G$, of the G-FET. The gate voltage can turn oscillations on and off and tune $f$ monotonically. As shown in Fig. 3c, no oscillations occur at the output when $V_G$ is set at zero. As $V_G$ increases to 0.68 V, the device starts to produce stable oscillations. For $V_G$ values varying from 0.68 to 1.80 V the frequency can be tuned monotonically from 1.42 to 1.04 MHz. As $V_G$ increases above 1.80 V the oscillations begin to show missing cycles, indicating that the bias setting exceeds the oscillation requirement. $V_{DC}$ is set at 3.65 V for these measurements. The tuning mechanism can be understood by examining the load line. As the slope of the load line changes with $V_G$ and falls within the red hatched region in Fig. 3d, oscillations appear at the output. The transfer characteristic of the G-FET is shown in the inset to Fig. 3d. Note that $V_{DS}$ is biased at 2.4 V, close to the value of the voltage drop across the G-FET when the circuit operates at $V_{DC}$ = 3.65 V. The charge neutrality point in this case is at 2.4 V, shifted by the large source–drain voltage of G-FET ($V_{DS}$). As $V_G$ increases from zero to 2.1 V, the resistance of the graphene channel monotonically increases, resulting in the oscillation frequency decreasing due to the increased RC time constant, where $R$ and $C$ are the effective resistance and capacitance, respectively. Figure 3e shows the gate



© 2016 Macmillan Publishers Limited, part of Springer Nature. All rights reserved.

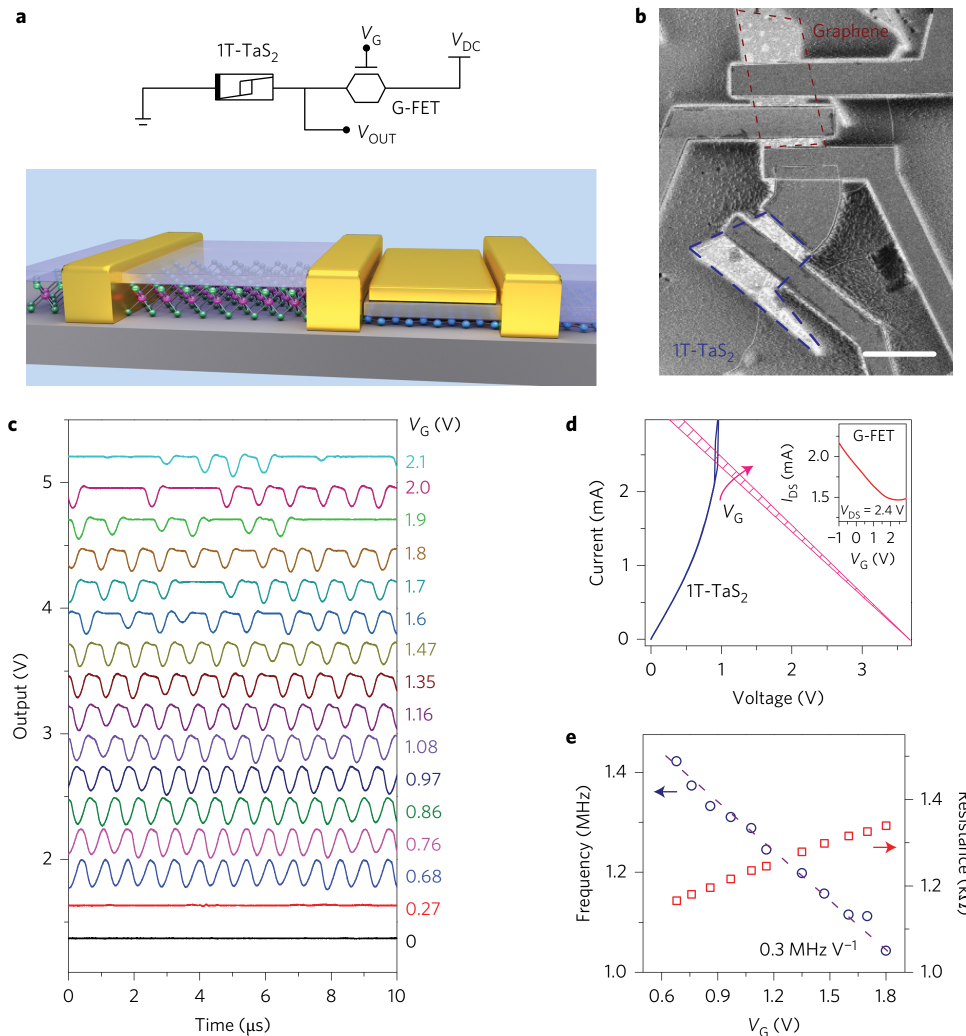


**Figure 3 | The integrated 1T-$TaS_2$–BN–graphene VCO. a**, Bottom: The device structure of the integrated oscillator consists of a G-FET series connected to 1T-$TaS_2$. Both the graphene and $TaS_2$ are fully covered with h-BN, which acts as a protective layer against oxidation for the 1T-$TaS_2$ and as a gate dielectric for the G-FET. The equivalent circuit and biasing set-up is shown in the top panel. The $V_{DC}$ bias is applied at the drain terminal of the G-FET and the $V_G$ bias is connected to the gate terminal of G-FET. The ground is connected to one terminal of 1T-$TaS_2$ device and the output port is common to both devices. **b**, The SEM image of the integrated 1T-$TaS_2$–BN–graphene VCO. The graphene and the $TaS_2$ are highlighted by dashed lines. Scale bar, 4 μm. **c**, Output waveforms at different gate biases when $V_{DC}$ is fixed at 3.65 V. The oscillation frequency is tunable with gate biases in the range of 0.68 V to 1.8 V. The different waveforms are vertically offset by 0.25 V for clarity. **d**, The load line representing the resistance range of the G-FET intersects with the *I*–*V* curve of the 1T-$TaS_2$ device. The arrow indicates the slope change of the load line with $V_G$. The inset shows the transfer characteristics (source–drain current, $I_{DS}$, as function of $V_G$) of the G-FET under a source–drain bias at 2.4 V. **e**, The dependence of the oscillation frequency on the gate bias. Blue circles show the frequency of the oscillation under an increased gate bias. The frequency can be adjusted monotonically with a tuning sensitivity of 0.3 MHz $V^{-1}$. The red squares are the resistance values of the G-FET under different gate biases with $V_{DC}$ = 2.4 V.

voltage tunablity of the oscillator frequency. The tuning sensitivity is 0.3 MHz $V^{-1}$, and the oscillation amplitude $V_{PP}$ is ~0.2 V. Control of both characteristics will improve dramatically as the technology for handling 2D materials advances.

The monolithic integration of a quasi-2D CDW channel with graphene has several advantages. The current carrying capacity of G-FETs[24] makes graphene a well-matched load to the low-resistance $TaS_2$. The oscillations occur when the IMT is triggered in 1T-$TaS_2$ in the mA range (for the 1–2 μm wide samples). With similar dimensions to 1T-$TaS_2$, graphene provides a well-matched current density and resistance. Owing to the linear resistance tunablity with the gate voltage of the G-FET at high $V_{DS}$ and high carrier concentrations, the frequency of the oscillator can be tuned linearly by $V_G$ over a wide range. The tuning linearity of VCOs is required for many practical applications[21]. An extra advantage of the CDW–G-FET integrated device is that G-FETs have been demonstrated to operate at very high frequencies of hundreds of GHz[25,26], which allows for increased oscillation frequencies. In our proof-of-concept measurements, the frequency is limited by the extrinsic RC time constants of the probe station. The intrinsic resistances and capacitances can be reduced by scaling. The graphene and h-BN layers in the device structure also act as heat spreaders owing to their high thermal conductivity[27,28].

From the circuit models in Figs 2a or 3a, the frequency is determined by the charging and discharging time of the capacitance, which is given by

$$1/f = T = C\left[\left(R_s//R_{di}\right)\ln(\alpha_i) - \left(R_s//R_{dm}\right)\ln(\alpha_m)\right] \quad (1)$$

where $\alpha_{m,i} = [V_{DC}-(1 + R_s/R_{dm,di})V_L]/[V_{DC}-(1 + R_s/R_{dm,di})V_H]$, m and i represent metallic and insulating states, respectively, $R_{di}$ is the resistance of $TaS_2$ in the insulating state, $R_{dm}$ is the resistance of



© 2016 Macmillan Publishers Limited, part of Springer Nature. All rights reserved.

$TaS_2$ in the metallic state, $R_s$ is the load resistance of either the resistor or the G-FET and $C$ is the lumped capacitance between the output node and the ground (Supplementary Fig. 7). $R_s//R_{di}$ is the parallel resistance of the $R_s$ and $R_{di}$. The intrinsic geometric capacitances and the resistivites of the 1T-$TaS_2$ film and the load resistor or transistor set the upper frequency limit of oscillation. The sheet resistivities of the 1T-$TaS_2$ in the high and low resistance states are 3 k$\Omega\,\square^{-1}$ and 740 $\Omega\,\square^{-1}$, respectively. These values are relatively low, allowing for extremely small RC time constants. Considering only the parallel plate capacitance to ground of the $TaS_2$ and graphene, the intrinsic RC-limited frequency given by equation (1) for the ~1 μm scale device shown in Fig. 3b is in the THz regime.

As the RC-limited frequency is so high, the intrinsic fundamental limit on the maximum frequency may be set by the time constants determined by the microscopic switching mechanism between the low- and high-resistance states. The voltage or current driven switching could result from the destruction of the Mott insulating state in the individual NC-CDW domains while leaving the lattice in the NC-CDW state (process a), or it could be accompanied by a reconstruction of the lattice from the NC-CDW state to the I-CDW state (process b). Process a is a purely electronic process and is therefore extremely fast. The speed of process b is governed by the time constant associated with the relaxation of the lattice. Available femtosecond ARPES data at room temperature suggest a time constant of 700 fs, which provides an upper frequency limit on the order of 1 THz (ref. 29). A lower frequency limit would result from a thermally induced switching mechanism whereby the current heats up the device sufficiently to induce the NC-CDW to IC-CDW transition. Such a mechanism is considered to be the most likely scenario in $VO_2$ devices[30,31]. At a fixed temperature, the NC-CDW to IC-CDW transition in samples of different lengths occurs at approximately constant electric fields and constant current densities (and therefore constant power densities). This indicates that thermal effects also play a role in the switching in our device. A study of $V_2O_3$ devices found that thermally induced switching could occur at subnanosecond timescales, resulting in GHz frequencies[32]. In either case, VCOs operating even at lower frequencies (for example, MHz in radio) are important devices with various applications[33]. Compact VCOs can also be used as elements in oscillator-based pattern-recognition neural networks[34,35].

The physical principles behind the operation of 1T-$TaS_2$ VCOs are different from those in the MITs used in $VO_2$ devices[36–42]. The transition in $VO_2$ is from the low-temperature monoclinic structure to the rutile structure[43–45]. The origin of the transition (Peierls versus Mott–Hubbard types) is under debate[43–45]. The transition in our 1T-$TaS_2$ devices is from NC-CDW to IC-CDW[46]. As $VO_2$ is a 3D material, the attempts to deposit it as thin films with small thicknesses ($H < 10$ nm) resulted in excessive strain and correspondingly reduced the phase transition temperature[47,48]. The phase transition from NC-CDW to IC-CDW in 6–9-nm-thin films of 1T-$TaS_2$ is almost the same as it is in the bulk (~350 K), well above room temperature[10].

## Methods

Methods and any associated references are available in the online version of the paper.

Received 29 February 2016; accepted 18 May 2016; published online 4 July 2016

## References

1. Grüner, G. *Density Waves in Solids* (Addison-Wesley, 1994).
2. Rossnagel, K. On the origin of charge-density waves in select layered transition-metal dichalcogenides. *J. Phys. Condens. Matter* **23,** 213001–213024 (2011).
3. Brown, S. & Grüner, G. Charge and spin density waves. *Sci. Am.* **270,** 50–56 (1994).
4. Thorne, R. E. Charge-density-wave conductors. *Phys. Today* **49,** 42–47 (1996).
5. Porer, M. *et al.* Non-thermal separation of electronic and structural orders in a persisting charge density wave. *Nature Mater.* **13,** 857–861 (2014).
6. Wilson, J. A., Di Salvo, F. J. & Mahajan, S. Charge-density waves and superlattices in the metallic layered transition metal dichalcogenides. *Phys. Rev. Lett.* **32,** 882–885 (1974).
7. Sipos, B. *et al.* From Mott state to superconductivity in 1T-$TaS_2$. *Nature Mater.* **7,** 960–965 (2008).
8. Stojchevska, L. *et al.* Ultrafast switching to a stable hidden quantum state in an electronic crystal. *Science* **344,** 177–180 (2014).
9. Manzke, R., Buslaps, T., Pfalzgraf, B., Skibowski, M. & Anderson, O. On the phase transitions in 1T-$TaS_2$. *Europhys. Lett.* **8,** 195–200 (1989).
10. Yu, Y. *et al.* Gate-tunable phase transitions in thin flakes of 1T-$TaS_2$. *Nature Nanotech.* **10,** 270–276 (2015).
11. Yoshida, M. *et al.* Controlling charge-density-wave states in nano-thick crystals of 1T-$TaS_2$. *Sci. Rep.* **4,** 7302 (2014).
12. Joe, Y. I. *et al.* Emergence of charge density wave domain walls above the superconducting dome in 1T-$TiSe_2$. *Nature Phys.* **10,** 421–425 (2014).
13. Samnakay, R. *et al.* Zone-folded phonons and the commensurate–incommensurate charge-density-wave transition in 1T-$TaSe_2$ thin films. *Nano Lett.* **15,** 2965–2973 (2015).
14. Hollander, M. J. *et al.* Electrically driven reversible insulator–metal phase transition in 1T-$TaS_2$. *Nano Lett.* **15,** 1861–1866 (2015).
15. Xi, X. *et al.* Strongly enhanced charge-density-wave order in monolayer $NbSe_2$. *Nature Nanotech.* **10,** 765–769 (2015).
16. Tsen, A. W. *et al.* Structure and control of charge density waves in two-dimensional 1T-$TaS_2$. *Proc. Natl Acad. Sci. USA* **112,** 15054–15059 (2016).
17. Yoshida, M., Suzuki, R., Zhang, Y., Nakano, M. & Iwasa, Y. Memristive phase switching in two-dimensional 1T-$TaS_2$ crystals. *Sci. Adv.* **1,** e1500606 (2015).
18. Wang, L. *et al.* One-dimensional electrical contact to a two-dimensional material. *Science* **342,** 614–617 (2013).
19. Doganov, R. A. *et al.* Transport properties of pristine few-layer black phosphorus by van der Waals passivation in an inert atmosphere. *Nature Commun.* **6,** 6647 (2014).
20. Cao, Y.-F. *et al.* Transport and capacitance properties of charge density wave in few-layer 2H-$TaS_2$ devices. *Chinese Phys. Lett.* **31,** 077203–077206 (2014).
21. Rhea, R. W. *Oscillator Design and Computer Simulation* (McGraw-Hill, 1997).
22. Razavi, B. A study of phase noise in CMOS oscillator. *IEEE J. Solid State Circ.* **31,** 331–343 (1996).
23. Stolyarov, M. A., Liu, G., Rumyantsev, S. L., Shur, M. & Balandin, A. A. Suppression of 1/*f* noise in near-ballistic h-BN-graphene-h-BN heterostructure field-effect transistors. *Appl. Phys. Lett.* **107,** 023106 (2015).
24. Novoselov, K. S. *et al.* Electric field effect in atomically thin carbon films. *Science* **22,** 666–669 (2004).
25. Lin, Y.-M. *et al.* Wafer-scale graphene integrated circuit. *Science* **332,** 1294–1297 (2011).
26. Wu, Y. *et al.* High-frequency, scaled graphene transistors on diamond-like carbon. *Nature* **472,** 74–78 (2011).
27. Balandin, A. A. Thermal properties of graphene and nanostructured carbon materials. *Nature Mater.* **10,** 569–581 (2011).
28. Jo, I. *et al.* Thermal conductivity and phonon transport in suspended few-layer hexagonal boron nitride. *Nano Lett.* **13,** 550–554 (2013).
29. Perfetti, L. *et al.* Femtosecond dynamics of electronic states in the Mott insulator 1T-$TaS_2$ by time resolved photoelectron spectroscopy. *New J. Phys.* **10,** 053019 (2008).
30. Kumar, S. *et al.* Local temperature redistribution and structural transition during joule-heating-driven conductance switching in $VO_2$. *Adv. Mater.* **25,** 6128–6132 (2013).
31. Zimmers, A. *et al.* Role of thermal heating on the voltage induced insulator-metal transition in $VO_2$. *Phys. Rev. Lett.* **110,** 056601 (2013).
32. Brockman, J. S. *et al.* Subnanosecond incubation times for electric-field-induced metallization of a correlated electron oxide. *Nature Nanotech.* **9,** 453–458 (2014).
33. Horowitz, P. & Hill, W. *The Art of Electronics* (Cambridge Univ. Press, 1989).
34. Hoppensteadt, F. C. & Izhikevich, E. M. Pattern recognition via synchronization in phase-locked loop neural networks. *IEEE Trans. Neural Netw.* **11,** 734–738 (2000).
35. Nikonov, D. E. *et al.* Coupled-oscillator associative memory array operation for pattern recognition. *IEEE J. Explor. Solid State Comput. Dev. Circ.* **1,** 85–93 (2015).
36. Rahman, M. H. & Hamid, M. A. K. Solid-state oscillator using a $VO_2$ polyconductor film as a circuit element. *Int. J. Electron.* **42,** 65–72 (1977).
37. Fisher, B. Voltage oscillations in switching $VO_2$ needles. *J. Appl. Phys.* **49,** 5339–5341 (1978).
38. Lee, Y. K. *et al.* Metal-insulator transition-induced electrical oscillation in vanadium dioxide thin film. *Appl. Phys. Lett.* **92,** 162903 (2008).
39. Leroy, J. *et al.* High-speed metal-insulator transition in vanadium dioxide films induced by an electrical pulsed voltage over nano-gap electrodes. *Appl. Phys. Lett.* **100,** 213507 (2012).
40. Shukla, N. *et al.* Synchronized charge oscillations in correlated electron systems. *Sci. Rep.* **4,** 4964 (2014).
41. Joushaghani, A. *et al.* Voltage-controlled switching and thermal effects in $VO_2$ nano-gap junctions. *Appl. Phys. Lett.* **104,** 221904 (2014).



© 2016 Macmillan Publishers Limited, part of Springer Nature. All rights reserved.

42. Wang, Y. *et al.* Electrical oscillation in Pt/$VO_2$ bilayer strips. *J. Appl. Phys.* **117,** 064502 (2015).
43. Yang, Z., Ko, C. & Ramanathan, S. Oxide electronics utilizing ultrafast metal-insulator transitions. *Annu. Rev. Mater. Res.* **41,** 337–367 (2011).
44. Pergament, A. *et al.* Vanadium dioxide: metal-insulator transition, electrical switching and oscillations. A review of state of the art and recent progress. Preprint at http://arxiv.org/abs/1601.06246 (2016).
45. Cavalleri, A. *et al.* Evidence for a structurally-driven insulator-to-metal transition in $VO_2$: a view from the ultrafast timescale. *Phys. Rev. B* **70,** 161102(R) (2004).
46. Petersen, J. C. *et al.* Clocking the melting transition of charge and lattice order in 1T–$TaS_2$ with ultrafast extreme-ultraviolet angle-resolved photoemission spectroscopy. *Phys. Rev. Lett.* **107,** 177402 (2011).
47. Paik, H. *et al.* Transport properties of ultra-thin $VO_2$ films on (001) $TiO_2$ grown by reactive molecular-beam epitaxy. *Appl. Phys. Lett.* **107,** 163101 (2015).
48. Quackenbush, N. F. *et al.* Nature of the metal insulator transition in ultrathin epitaxial vanadium dioxide. *Nano Lett.* **13,** 4857–4861 (2013).

## Acknowledgements

Nanofabrication and device testing were supported, in part, by the National Science Foundation (NSF) and Semiconductor Research Corporation (SRC) Nanoelectronic Research Initiative (NRI) for Project 2204.001 'Charge-Density-Wave Computational Fabric: New State Variables and Alternative Material Implementation' (NSF ECCS-1124733) as a part of the Nanoelectronics for 2020 and beyond (NEB-2020) programme and by the Semiconductor Research Corporation (SRC) and Defense Advanced Research Project Agency (DARPA) through STARnet Center for Function Accelerated nanoMaterial Engineering (FAME). Material synthesis and device simulations were supported by the Emerging Frontiers of Research Initiative (EFRI) 2-DARE project 'Novel Switching Phenomena in Atomic $MX_2$ Heterostructures for Multifunctional Applications' (NSF 005400).

## Author contributions

A.A.B. coordinated the project and contributed to the experimental data analysis; R.K.L. led the theoretical analysis; T.T.S. supervised the material synthesis and contributed to the characterization of the materials; G.L. designed, fabricated and tested the devices and analysed the experimental data; T.R.P. synthesized $TaS_2$ crystals; B.D. conducted computer simulations. All authors contributed to writing the manuscript.

## Additional information

Supplementary information is available in the online version of the paper. Reprints and permissions information is available online at www.nature.com/reprints. Correspondence and requests for materials should be addressed to A.A.B.

## Competing financial interests

The authors declare no competing financial interests.



© 2016 Macmillan Publishers Limited, part of Springer Nature. All rights reserved.

## Methods

**1T-$TaS_2$ crystal growth.** $TaS_2$ crystals were grown by an adapted chemical vapour transport method, where the 1T polytype can be isolated by fast quenching from the crystal growth temperature (875–975 °C; ref. 49). Elemental tantalum (20.4 mmol, Sigma-Aldrich 99.99% purity) and sulfur (41.1 mmol, J.T. Baker >99.9% purity) were ground with mortar and pestle and placed in a 17.8 × 1.0 cm fused quartz ampoule (cleaned by soaking overnight in nitric acid followed by annealing at 900 °C for 24 h). Elemental iodine (J.T. Baker 99.9% purity) was added (~88 mg for an ampoule with a volume of ~14.0 $cm^3$). The ampoule was evacuated and backfilled three times with argon, with cooling to mitigate $I_2$ sublimation. Next the ampoule was flame-sealed and heated in a two-zone tube furnace at 10 °C $min^{-1}$ to 975 °C (the hot zone) and 875 °C (the cool zone). These temperatures were held for one week. Then the ampoule was removed from the hot furnace and immediately quenched in a water–ice–NaCl bath. The resulting golden crystals, shown in Supplementary Fig. 1, were characterized as detailed below. The as-grown crystals and their atomic structure are shown in Supplementary Fig. 1. The structure and phase purity were verified by powder X-ray diffraction (shown in Supplementary Fig. 2) and the stoichiometry was confirmed with energy dispersive spectroscopy and electron probe microanalysis (shown in Supplementary Fig. 3 and Supplementary Table 1).

**Electrical characteristics of the 1T-$TaS_2$ devices.** All $I$–$V$ characteristics were measured in the Lakeshore cryogenic probe station TTPX with a semiconductor analyser (Agilent B1500). The oscillator of the waveform is collected by an oscilloscope (LeCroy WaveAce1012) whereas the d.c. voltage supply of the circuit is biased with a BK Precision 1787B.

## References

49. Lieth, R. M. A. & Terhell, J. C. J. M. in *Preparation and Crystal Growth of Materials With Layered Structures* Vol. 1 (ed. Lieth, R. M. A.) 186 (Springer, 1977).



© 2016 Macmillan Publishers Limited, part of Springer Nature. All rights reserved.